ACS NANO

www.acsnano.org

Article

Lamellar Composites of Vertical Graphene and Phase-Change Materials for Highly Efficient Heat Dissipation

Xiaoqian Teng, Chuanren Ye,* Shantao Zhang, and Yanwu Zhu*

Cite This: *ACS Nano* 2026, 20, 2239−2247

Read Online

ACCESS | Metrics & More | Article Recommendations | Supporting Information

ABSTRACT: High-performance thermal interface materials (TIMs) often encounter the trade-off between high thermal conductivity and superior compliance. Herein, we report a graphene-based lamellar composite consisting of vertical graphene films and modified paraffin wax, fabricated by a layer-by-layer rolling assembly. Owing to the excellent deformability and confined flow of melted paraffin wax between graphene films, the composite shows a low contact thermal resistance of 17 K mm^2 W^{-1} at 60 psi as a heat transfer interface, without leakage of paraffin wax. Due to the synergistic effect between the high heat capacity of paraffin wax and the high thermal conductivity of graphene films, the composite TIM yields an ultrahigh overall thermal conductivity of 789 W m^{-1} K^{-1} at 55 °C. When tested under a heat flux density of 30 W cm^{-2} on a simulated chip, the lamellar composite demonstrates a temperature rise much lower than that of a commercial TIM pad. The superior cooling efficiency indicates that the lamellar composite potentially offers a scalable and finely controllable design protocol for advanced TIMs to meet high-power heat dissipation requirements.

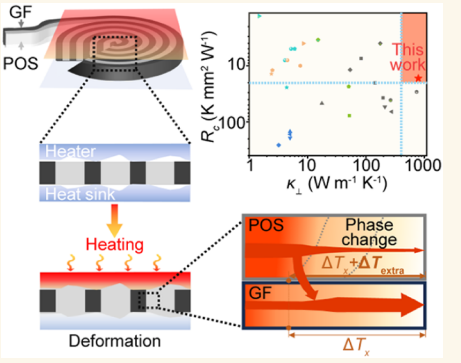

KEYWORDS: *thermal interface materials, high thermal conductivity, graphene, contact thermal resistance, phase-change materials*

The booming integration of transistors and miniaturization of chip configurations have greatly elevated the output power per unit area, thereby raising concerns about the operating temperature, which largely influences the failure rate of chips.[1−3] Thermal interface materials (TIMs), filling the gap between the chip and the heat sink, are employed to reduce the heat barrier originating from the very low thermal conductivity of air (~0.026 W m^{-1} K^{-1}).[4] For intimate contact with chips and efficient heat dissipation, advanced TIMs simultaneously require high vertical thermal conductivity ($\kappa_\perp$) and low contact thermal resistance (R_c), accompanied by low compressive modulus, great conformability, low bonding line thickness, and excellent interface matching.[5] In practical design, the trade-off between thermal conductivity and contact thermal resistance emerges as a severe challenge in the development of candidate materials, while the mechanical and bonding properties of TIMs impact the thermal resistance on interface. For instance, silicone and thermally conductive filler-based pasty thermal greases (5−20 K mm^2 W^{-1}) exhibit superior interfacial contact compared to thermal pads (30−200 K mm^2 W^{-1}), but both are limited by the low thermal conductivity of polymers (<17 W m^{-1} K^{-1}).[6] Phase-change materials (PCMs), such as paraffin wax (PW), polyethylene glycol, and polyurethane,[7] show favorable thermal resistance of 5−70 K mm^2 W^{-1} due to the good adhesion of melted flow and ultrahigh heat storage capacity during phase transition.[6,8] However, the even lower thermal conductivity of PCMs (1−10 W m^{-1} K^{-1}) is insufficient for the dissipation of high heat flux, and leakage remains a concern for operational reliability.[6,7]

To improve the thermal conductivity of TIMs, the incorporation of high thermal conductivity fillers into the polymer matrix has been accepted as an efficient approach. Conventional inorganic fillers like Al_2O_3 (30−40 W m^{-1} K^{-1}), AlN (150−200 W m^{-1} K^{-1}), and BN (29−300 W m^{-1} K^{-1})[6] typically require a high filling fraction of up to 40−70 wt % for a significant elevation in the thermal conductivity of composites.[9,10] In comparison, nanocarbons such as graphene (1689−5300 W m^{-1} K^{-1} in-plane),[11−13] carbon nanotubes (3000−3500 W m^{-1} K^{-1} along the axial direction),[14,15] carbon fibers (900−1100 W m^{-1} K^{-1} along the axial direction),[16] and graphene fibers (232−1660 W m^{-1} K^{-1} along the axial direction)[17,18] can build interconnected frameworks at a much lower filling content (5−10 wt %) due to their huge specific surface areas.[19,20] However, due to their high anisotropy in thermal conductivity, nanocarbons often need to be precisely controlled in terms of distribution and orientation to ensure efficient thermal dissipation along the desired direction.[21] In this regard, vertical graphene (VG) can potentially act as a promising filler when the vertical direction aligns with the heat dissipation direction in TIMs. Assembled from graphene

Received: October 10, 2025
Revised: January 1, 2026
Accepted: January 2, 2026
Published: January 8, 2026

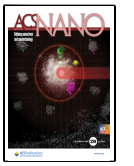

https://doi.org/10.1021/acsnano.5c17391
ACS Nano 2026, 20, 2239−2247

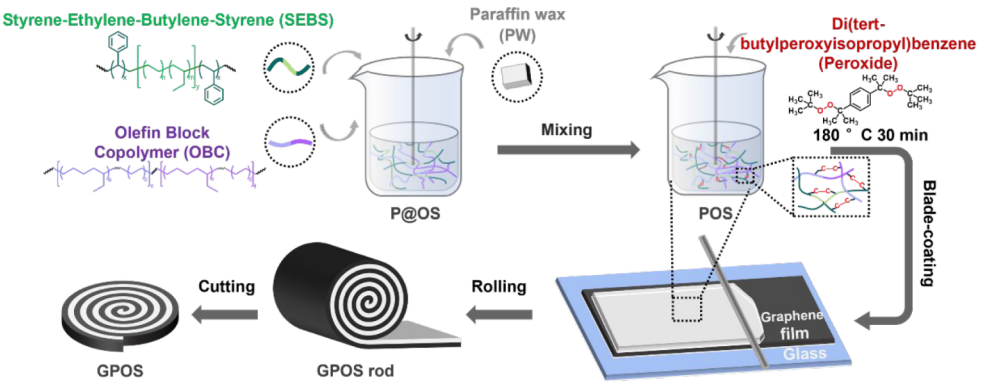

Figure 1. Schematic of the preparation process of GPOS.

platelets, VG can be fabricated through template-assisted methods such as directional freeze-drying[22] or external field manipulation.[23] Grown from gaseous sources, VG can also be obtained by oriented growth, e.g., with plasma-enhanced chemical vapor deposition.[24] However, due to the loose framework or the existence of defects in the VG obtained through these methods, the vertical thermal conductivity $\kappa_{\perp}$ has been limited to a range of 20−54 W m^{-1} K^{-1}.[22,24,25]

In contrast, obtained from the assembly, reduction, and graphitization of graphene oxide platelets, highly ordered graphene films (GFs) exhibit a very high in-plane thermal conductivity of up to 2000 W m^{-1} K^{-1}, allowing for the extensive applications of GFs in heat dissipation of portable electronic devices.[26,27] When the thick GFs are cut into slices and turned around, vertically aligned GFs (VAGFs) can be used for superior thermal conduction along the vertical direction.[28] By adhering GFs to a prestretched polyacrylate substrate and then releasing the tension to crimp the film, a VAGF has been prepared with a $\kappa_{\perp}$ of 143 W m^{-1} K^{-1} and a good compressibility (compressive strain ∼9.9% at 10 psi (∼68.9 kPa)).[29] When combined with polymers, the composite like VAGF/polydimethylsiloxane made by vacuum-assisted impregnation, exhibits a high $\kappa_{\perp}$ of 615 W m^{-1} K^{-1} but with inferior compressibility (compressive strain ∼0.075% at 10 psi) compromising the effective contact.[30] Due to their fluidity, liquid metals are also employed to improve interfacial contact and reduce thermal resistance, such as in TIMs containing encapsulated liquid metal microspheres.[31,32] To alleviate the rigid edge of graphene stacking, liquid gallium has been deposited as a cap layer and significantly reduces R_c from 82 to 6 K mm^2 W^{-1}, approaching the performance of commercial thermal grease,[33] but the etching of Al and Cu on embrittlement and the potential leakage of liquid metals remain concerns.[34,35] To construct a deformable surface, a structure of VAGF composite made by the inward shrinkage of the silver paste component to expose the loose vertical graphene caps, has presented $\kappa_{\perp}$ of 739 W m^{-1} K^{-1} and R_c of 29 K mm^2 W^{-1}, the latter of which is close to that of thermal pad (30−200 K mm^2 W^{-1}).[36] Simultaneously achieving the optimization of thermal conductivity and contact thermal resistance for ultrahigh $\kappa_{\perp}$ (>400 W m^{-1} K^{-1}) and very low R_c (<20 K mm^2 W^{-1}) is still an urgent requirement for developing high-performance graphene-based TIMs.

Herein, we present a lamellar composite made by layer-by-layer rolling assembly of GFs with shape-stabilized PW. Obtained by cutting the round-shaped rolls into thin slices, the VAGF/PW composite shows exceptional deformability due to the recyclable melting/solidification of modified PW, promoting a large compression strain of 9.3% at 10 psi and a low R_c of 17 K mm^2 W^{-1} at 60 psi. Real-time infrared (IR) monitoring and numerical simulation verify that the phase change of modified paraffin induces significant heat redistribution within the composite, generating an internal temperature gradient on GF. Benefiting from the extra temperature gradient and large latent heat release during phase transition, rapid heat dissipation is realized via GF with high thermal conductivity, achieving an ultrahigh $\kappa_{\perp}$ of 789 W m^{-1} K^{-1} at 55 °C. In a prototype testing under a heat flux of 30 W cm^{-2}, the composite TIM demonstrates a temperature rise of 30 °C on the simulated chip, much smaller than that of commercial carbon fiber or graphene thermal pads. Our research provides a strategy for the synergistic enhancement of heat transfer efficiency by combining high heat capacity and high heat conduction for next-generation thermal management.

RESULTS AND DISCUSSION

Preparation and Characterization of VAGF/PW Composites

The preparation of VAGF/PW composite TIMs is illustrated in Figure 1, which starts with the modification of PW to overcome possible leakage during application. To modify the PW, olefin block copolymer (OBC) and styrene−ethylene−butene−styrene (SEBS) were incorporated into the paraffin matrix to construct a physically mixed polymer composite (P@OS), followed by introducing di(*tert*-butylperoxyisopropyl)-benzene for the chemical cross-linking of OBC/SEBS molecular chains to form a cross-linked composite (POS).[37] The enhanced intensities of Raman peaks at 1132 cm^{-1} (C−C symmetric stretching) and 1295 cm^{-1} (CH_2 twisting) for POS compared with P@OS (Figure S1) indicate the formation of C−C bonds between OBC and SEBS chains, a sign of successful cross-linking.[38] Upon forming the interconnected polymer backbone, POS demonstrates great deformability and controlled flowability, e.g., by controlling temperature, which allows for the uniform blade coating on the large-area GFs to fabricate a lamella consisting of GFs and POS with a controllable fraction of GF/POS. The obtained composite film of GF/POS was then stacked by rolling into a dense cylindrical assembly and subjected to cutting by a mechanical blade. The thickness of the slices is controlled at predetermined values for the heat transfer of such TIMs along the direction perpendicular to the in-plane direction of

https://doi.org/10.1021/acsnano.5c17391
ACS Nano 2026, 20, 2239−2247

GF/POS films, leading to slice samples designated as GPOS thereafter.

By adjusting the doctor-blade thickness, three samples with different POS loadings on 40-μm-thick GFs were obtained (Figure 2a), named as GPOS1, GPOS2, and GPOS3, corresponding to POS volume percentages of 44.5%, 73.2%, and 80.5%, respectively. Obtained by cutting as described above, GPOS disks with diameters of ~10 mm were fabricated, as shown in the inset of Figure 2a. The structures and mechanical properties of GPOS samples were further analyzed. Figure 2b shows the Raman spectra of GF and GPOS2, where the presence of G (1582 cm^{-1}) and 2D (2722 cm^{-1}) modes, together with the barely detectable D mode (I_D/I_G = 0.035) in the Raman spectrum of GF, confirms the high-quality graphene in GFs. This peak and the characteristic peak of POS located at 2884 cm^{-1} are also observed at the junction between GF and POS in GPOS2 without a significant enhancement of the D peak intensity, demonstrating the van der Waals contact instead of covalent interfacial bonding between GF and POS. A three-dimensional (3D) X-ray tomography (Figure 2c) of GPOS1 disk clearly reveals a densely packed composite assembly yet with the uniform spatial distribution of GF and POS. Enlarged images (Figure 2d-f) further demonstrate the zebra-like and intimate lamellar architecture without cavities or agglomeration in GPOS samples, in which the thickness of POS layer increases from 33 ± 2 μm for GPOS1 to 103 ± 10 μm for GPOS2, and 163 ± 11 μm for GPOS3. These thickness values of POS, combined with that of GF, closely match the thickness of the POS-loaded GF laminate in Figure 2a prior to the rolling assembly.

To confirm the leakage prohibition of PW modified by the introduced polymer skeleton, cycling leakage testing of GPOSs has been carried out in a temperature range of 25−75 °C. Figures 2g and S2 show that the leaking weight increases with the fraction of POS in the composite, but even that of GPOS3 or pure POS is less than 0.3 and 1.2 wt % after 300 cycles, respectively, demonstrating the favorable mass stability upon melting. The exceptional antileakage capability of GPOSs under pressures of 10−40 psi is also confirmed by the negligible leakage of less than 0.6 wt % (Figure S3). When heated from room temperature to 80 °C, GPOSs and POS slices maintain shape integrity well, in great contrast to the complete flowing upon melting of the original PW (Figure S4). With great mass stability and thermal conformability, the POS

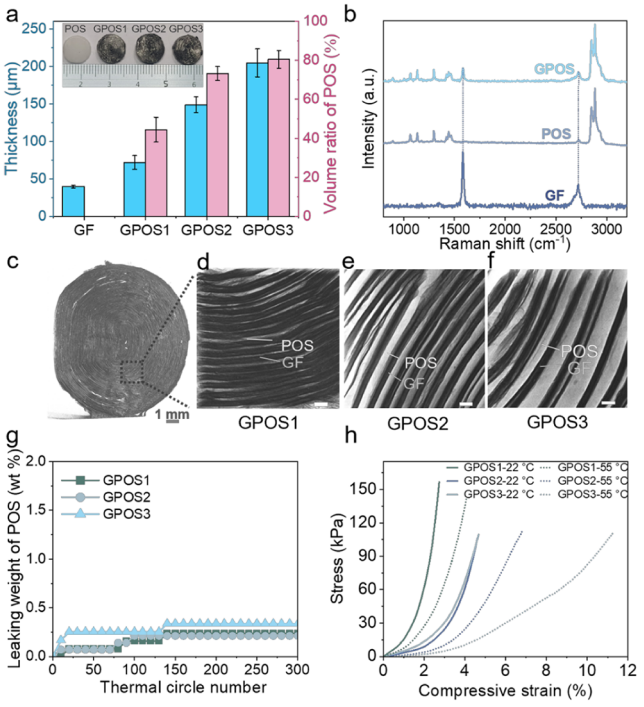

Figure 2. Structural and mechanical characterizations of GPOSs. (a) Thickness of the POS-coated VG laminate composite before rolling and the volume ratio of POS in GPOSs. Inset shows photographs of POS and GPOSs. (b) Raman spectra of GF, POS, and GPOS2. 3D X-ray tomography images of (c) GPOS1 in an overview, (d) GPOS1, (e) GPOS2, and (f) GPOS3 in enlarged views. Scale bar: 100 μm. (g) Leaking weight of GPOSs during 300 melting/freezing cycles. (h) Compressive strain−stress curves of GPOSs at 22 and 55 °C.

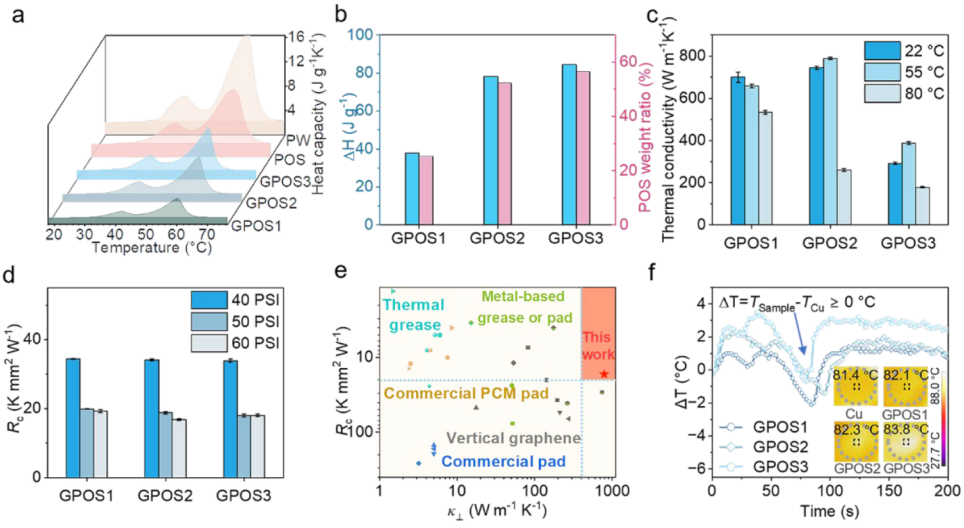

Figure 3. Thermophysical characterization of GPOS samples. (a) DSC curves of PW, POS, and GPOSs. (b) Enthalpy of fusion and calculated weight ratio of POS in GPOSs. (c) Vertical thermal conductivity $\kappa_\perp$ of GPOSs at 22, 55, and 80 °C. (d) Contact thermal resistance of GPOSs under compressive stress. (e) Comparison of $\kappa_\perp$ and R_c of GPOS2 measured at 55 °C with previously reported and commercial TIMs. (f) Surface temperature difference between GPOSs and copper versus heating time. Insets show IR images of GPOSs and copper after being heated for 200 s.

https://doi.org/10.1021/acsnano.5c17391
ACS Nano 2026, 20, 2239−2247

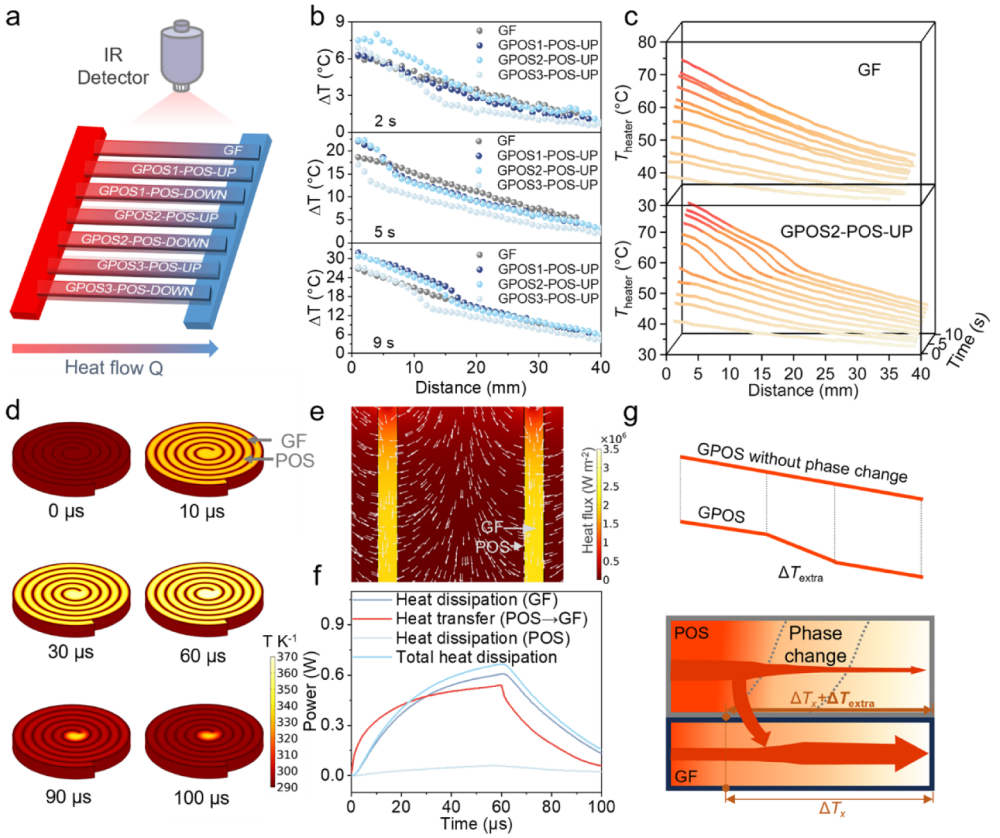

Figure 4. Heat transfer mechanism of GPOSs. (a) Schematic of the hot bridge apparatus with IR temperature monitoring. (b) Temperature difference recorded for GF and the POS side of GPOSs lamellae after 2, 5, and 9 s. (c) Temperature of GF and GPOS2-POS-UP from 0 to 10 s. (d) Numerical modeling of temperature evolution of GPOS2 with a heating power applied for 60 μs. (e) Heat flux distribution and heat transport direction in GPOS2. (f) Integrated heat dissipation and heat exchange power for graphene and POS. (g) Schematic of the heat transfer mechanism for GPOSs.

in GPOSs retains favorable flexibility as the temperature rises. Compression experiments performed at 55 °C (please note the melting of POS starts at ∼51 °C and peaks at ∼65 °C) reveal compressive strains of 3.1%, 5.6%, and 9.3% for GPOS1, GPOS2, and GPOS3 at 10 psi, respectively, which are increased by 46.9%, 35.9%, and 130.4% compared with those in the solid state (22 °C) under the same pressure (Figure 2h). The improved deformability of GPOS samples at 55 °C can be attributed to the liquid state of POS, where the chain-softening transformation occurs in OBC and SEBS molecules.[37] The compression strains of GPOSs are further increased at temperatures above the melting point (80 °C, Figure S5a) for the same compression stress to a value of 9.3% for GPOS2, which is comparable to the highest values previously reported and those of commercial TIMs (Figure S5b). The good conformability of GPOSs would facilitate close interfacial contact between the chip and heat sink under pressure. Furthermore, GPOS1 maintains nearly unchanged stress−strain profiles after 100 compression cycles (Figure S6a), while GPOS2 and GPOS3 exhibit consistent mechanical behavior across 10 cycles (Figures S6b-S6c), demonstrating exceptional structural stability and long-term reliability.

Thermophysical Characterization of GPOS

The thermophysical properties of GPOSs are characterized to evaluate their interfacial heat transfer capacity. The differential scanning calorimeter (DSC) curves as presented in Figure 3a demonstrate that the phase transition of GPOSs spans a broad temperature range of 32−69 °C, aligning with operational temperatures of commercial chips from room temperature to ∼70 °C.[39] The two dominant endothermic peaks of GPOSs and POS share the same positions and shape with PW, suggesting that the heat storage capacity of GPOS is inherited from PW, while irrelevant to the phase change of SEBS and OBC due to their high melting points (160 °C for SEBS and 100 °C for OBC).[40,41] Into the details, the peak at ∼42 °C or at ∼60 °C is, respectively, affiliated with a solid−solid phase transition (ordered-disordered arrangement of molecular chains) or a solid−liquid phase transition of paraffin molecules.[42] As seen in Figure 3b, the increased mass percentage of POS leads to an elevation of latent heat from 38 J g^{-1} for GPOS1 to 84 J g^{-1} for GPOS3. Three temperatures, 22, 55, and 80 °C, corresponding to the solid state, phase transition state, and liquid state of POS, respectively, have been selected for the thermal diffusivity measurement of GPOSs by the laser flash method. As presented in Figure S7, with more POS, the thermal diffusivity of GPOSs at 22 °C initially increases from 637 mm^2 s^{-1} (GPOS1) to 650 mm^2 s^{-1} (GPOS2) and then decreases to 229 mm^2 s^{-1} (GPOS3) at 22 °C. The measurement at 55 °C shows a similar trend. In contrast, the thermal diffusivity of GPOSs measured at 80 °C shows a monotonous decrease from 430 mm^2 s^{-1} (GPOS1) to 138 mm^2 s^{-1} (GPOS3). With values of sample density and heat capacity (Figure S8),[43,44] the thermal conductivity $\kappa_{\perp}$ of GPOSs aligns well with the thermal diffusivity, as presented in Figure 3c, demonstrating a record-high value of 789 W m^{-1} K^{-1} at 55 °C (745 W m^{-1} K^{-1} @ 22

https://doi.org/10.1021/acsnano.5c17391
ACS Nano 2026, 20, 2239−2247

°C) for GPOS2. The anomalous elevation of thermal diffusion/conductivity for GPOS2, which contradicts the expectation of a monotonous decrease trend for graphene composites at room temperature, is clearly correlated to the phase change of POS.

The contact thermal resistance has been evaluated at pressures of 40−60 psi and 55 °C to determine the interfacial heat transfer performance using the ASTM D5470 standard, as illustrated in Figure S9.[33] Figures 3d and S10 show that the contact thermal resistance (R_c) and total thermal resistance (R_{total}) of GPOSs decrease with the pressure applied. The R_c value at 50 psi sharply drops for all the GPOS samples compared to those obtained at 40 psi due to sufficient thermal contact under the higher pressure. At 60 psi, all GPOS samples show close R_c values, indicating that the POS fraction in the range of 44.5−80.5 vol % can effectively deform and fill the gap to bridge graphene lamellas and the heat source. Notably, a low R_c of 17 K mm^2 W^{-1} for GPOS2 is obtained at 60 psi. As summarized in Figure 3e and Table S1, GPOS2 exhibits the highest thermal conductivity among the reported TIMs and commercially available products, and the exceptional contact thermal resistance (17 K mm^2 W^{-1}) is superior or comparable to commercial thermal pads and vertically aligned graphene.[24,28,29,33,36,45−51] In addition, the thermal transfer of GPOSs and the Cu disk was compared by monitoring infrared (IR) images during simultaneous heating, with their temperature profiles recorded in Figure S11. The temperature difference between GPOSs and Cu (Figure 3f) reveals that GPOSs overall maintain a faster temperature increase and a higher temperature than Cu across the entire heating duration, except for the transient temperature inversion between 64 and 100 s, where GPOSs exhibit a temperature of 0−2 °C lower than Cu. The inversion correlates with the endothermic phase transition, consistent with DSC results. The insets of Figure 3f visually demonstrate the surface temperature of GPOSs higher than that of Cu by 1−3 °C after heating for 200 s.

Heat Transfer Mechanism of GPOS

To reveal the mechanism of phase change enhancement in heat transfer, the temperature of both sides of GF/POS strips before rolling was monitored on a hot bridge apparatus with an IR detector to obtain the dynamic temperature distribution of GPOSs or GF, as depicted in Figure 4a. To perform the monitoring, the GF/POS lamella strips were attached to two copper blocks, and a thermal gradient was then established along the strips by heating one copper block while using the other one as the heat sink. Surface temperature acquired on POS side or on graphene side is defined as POS-UP (with POS side exposed to the IR detector) or POS-DOWN (with GF side exposed to the IR detector), respectively. Figure 4b shows the temperature profiles taken from GPOSs-POS-UP and bare GF across the thermal gradient, and Figure S12 presents the corresponding IR images. From Figure 4b we can see that the temperature rise of GPOS2 exceeds that of GPOS1 at 2 s, then gets close afterward, and both GPOS1 and GPOS2 significantly surpass the value of GPOS3. The higher temperature rise indicates a faster heat transfer speed, which can be attributed to the superior thermal conductivity of GPOS1 and GPOS2 compared to that of GPOS3. Interestingly, GPOS2 achieves a temperature rise higher than that of GF, while GPOS1 and GPOS3 align with the GF near the heat source for 2 s in contrast to the close or slightly lower temperature rise of GPOSs compared with GF at the cooling end. At the moment of 5 or 9 s, it can be observed that the POS sides of GPOS1 and GPOS2 show higher temperatures than bare GF near the heating source, with sudden declines in the middle region. The temperature range corresponding to the decline is consistent with the solid−liquid phase change temperature of POS (~46−63 °C). By comparing the whole heating duration of 10 s for bare GF and POS-UP of GPOS2 (Figure 4c), we can see that the bare GF retains a nearly linear temperature distribution along the distance, while the temperature of GPOS2 shows a significant drop at a certain position, which evolves with time, suggesting a forward phase transition frontline propagating away from the heating source. In contrast to the negligible heat transfer in the heat bridge of bare POS (Figure S13) due to the low thermal conductivity (~0.2 W m^{-1} K^{-1}, Figure S14), the temperature rise of GPOSs near the heating source is clearly related to the synergistic effect of GF and POS in GPOSs.

Finite-element model with continuous heating for 60 μs was built to elucidate the thermal transport based on the structural parameters of GPOS2. The temperature evolution upon heating and cooling is shown Figure 4d, from which we can see that POS exhibits a higher temperature region than GF, indicating that heat is accumulated in POS and the transfer to GF is more efficient due to the high thermal conductivity and low capacity of GF (<1 J g^{-1} K^{-1}, Figure S14). The temperature of GPOS-POS-UP was higher than that of GPOS-POS-DOWN (Figure S15) and the heat flux and temperature from POS to GF further confirm the role of POS as a heat reservoir, while the substantial heat flux through GF demonstrates a highway of heat conduction for GF (Figure 4e and Figure S16). Figure 4f quantitatively analyzes the heat dissipation in GF or POS and the heat transfer at the GF/POS interface. From the curves we can see that the heat transfer from the POS to GF dominates at the beginning of 20 μs, and then GF-mediated thermal dissipation becomes predominant after 28 μs. In this process, the heat dissipation in POS remains at a very low level, and GF-POS interfacial resistance exerts a limited impact on heat transfer (Figure S17). Figure 4g summarizes the heat transfer mechanisms in GPOS. In such a process, the heat absorption of POS with high heat capacity and phase-changing latent heat provides a sufficient heat supply to GF under an extra temperature gradient (ΔT_{extra}), which is induced by phase transition of POS and determined by POS content. According to Newton's law of cooling, the heat transfer rate is proportional to the temperature difference:

$$\frac{dQ}{dt} \propto -(\Delta T + \Delta T_{extra}) \quad (1)$$

where Q is the heat of transfer and t is time. Therefore, ΔT_{extra} generated from the temperature redistribution prompts the local heat transfer speed in GPOS. Then the high thermal conductivity GF, acting as a heat transfer highway, delivers the heat from POS. The unique enhancement in heat transfer of POS is balanced with the amount of heat dissipation channels represented by GF content, yielding a nonmonotonic relationship between the thermal conductivity of GPOS and POS volume ratio, which reaches a maximum for GPOS2.

TIM Performance of GPOS

To evaluate the practical performance of GPOSs, a heater and a copper heat sink were used to simulate the electronic packaging environment at a pressure of 10 psi, as shown in

https://doi.org/10.1021/acsnano.5c17391
ACS Nano 2026, 20, 2239−2247

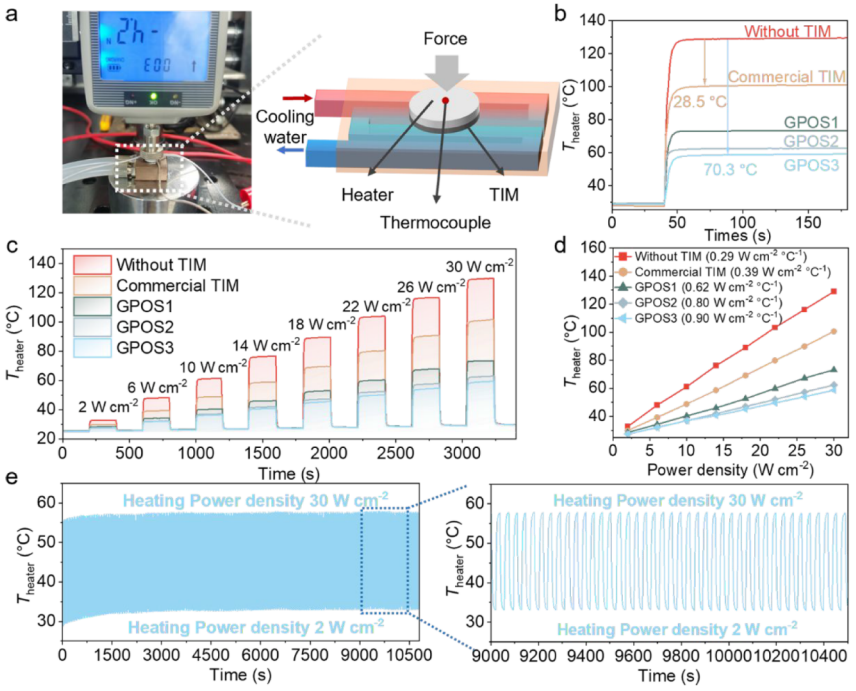

Figure 5. Heat dissipation performance of GPOSs. (a) Experimental setup and schematic configuration of the heat dissipation evaluation. (b) Curve of T_{heater} versus time with an input of 30 W cm^{-2}. (c) Steady-state T_{heater} versus the input power density from 2 to 30 W cm^{-2}. (d) T_{heater} values versus power density. (e) Thermal cycling stability of GPOS3.

Figure 5a. Figure 5b shows that, with an input power of 30 W cm^{-2}, the surface temperature of the heater (T_{heater}) rises by 30−44 °C above room temperature for GPOSs, all significantly lower than the rise of 73 °C for the commercial carbon fiber thermal pads. Notably, GPOS3 reduces T_{heater} by 70 °C compared to heat dissipation without TIM, by 42 °C relative to the commercial carbon fiber TIM, and by 23.1 °C against the commercial graphene TIM (Figure S18), highlighting its superior heat dissipation efficiency. By measuring the temperature rise for input powers from 2 to 30 W cm^{-2} in Figure 5c, GPOSs demonstrate exceptional heat dissipation stability and efficiency, outperforming the situation without TIM or with commercial TIM. These steady-state T_{heater} and power density exhibit a linear relationship and produce the equivalent heat dissipation coefficients, as calculated by the reciprocals of the slope in Figure 5d. GPOSs exhibited a heat dissipation coefficient of 0.6−0.9 W cm^{-2} °C^{-1}, obtaining a 59.0−130.8% improvement over the commercial TIM. The low temperature increase and high heat dissipation coefficient demonstrate the superior heat transfer performance of GPOSs in practical applications. Finally, we evaluated the thermal cycling stability of GPOSs by alternating the heating power between 2 and 30 W cm^{-2}. After 3600 thermal cycles, each with a period of 3 s, the stable temperature rise proves the long-term heat dissipation stability of GPOS3 (Figure 5e) and GPOS1/GPOS2 (Figure S19), proving their compatibility for repeated thermal shock in practical applications.

CONCLUSIONS

In summary, we propose a potentially scalable, controllable, and cost-effective preparation of graphene-based lamellar composites. The dense, roll-type assembly of macroscopic graphene films with a modified paraffin wax layer is confirmed to facilitate efficient heat transfer without leakage issues. The high compliance of modified paraffin wax in the phase-changing range effectively mitigates the contact thermal resistance and results in a low R_c of 17 K mm^2 W^{-1}. The IR monitoring and numerical simulation confirm that the large latent heat from the phase change of paraffin can redistribute the temperature gradient inside the graphene composite and drive a higher thermal conduction. As a result, a high thermal conductivity of 789 W m^{-1} K^{-1} at 55 °C is realized in such a graphene-based composite. The scalable and controllable rolling potentially enables intelligent design and precise preparation of the laminar architecture. Our finding highlights the potential for broader applications of graphene films combining phase-change materials in high-performance thermal management.

METHODS

Materials

The graphene films with an average thickness of 40 μm were purchased from Changzhou Fuxi Technology Co., Ltd., and the basic properties are shown in Table S2. The paraffin wax was purchased from Shanghai Yiyang Instrument Co., Ltd. Di(*tert*-butylperoxyisopropyl)benzene ($C_{20}H_{34}O_4$, 96%, mixture of isomers) was purchased from Shanghai Macklin Biochemical Co., Ltd. OBC (INFUSETM 9530) and SEBS (FG1901, 30/70) were acquired from Dow Chemical Company and Kraton Corporation.

Synthesis of P@OS, POS, and GPOS

P@OS was synthesized through a sequential blending process. First, 3.75 g of SEBS and 30 g of PW were melted at 150 °C and blended by stirring at 200 rpm to form a gel. The stirring speed was reduced to 100 rpm before the addition of 3.75 g of OBC, and a homogeneous mixture of P@OS was obtained after thorough blending. With the temperature raised to 180 °C, 0.25 g of di(*tert*-butylperoxyisopropyl)-benzene was added to the mixture and reacted for 30 min to yield POS. For the preparation of GPOS, a graphene film was tightly attached to a hot plate and preheated to 120 °C to ensure good flowability of POS. The blade-coating of POS was conducted with various coating thicknesses, corresponding to changeable composite

https://doi.org/10.1021/acsnano.5c17391
ACS Nano 2026, 20, 2239−2247

ratios, to obtain the original lamellar composite. GPOS rolls were fabricated by rolling the lamellae and then cutting into the targeted GPOS slices.

Leakage Testing

Leakage of GPOSs was evaluated by measuring the mass change during cycled heating and cooling between 75 and 25 °C. The shape retention of PW, POS, and GPOS was recorded and compared under a heating temperature ranging from room temperature to 80 °C.

Thermal Conductivity

The thermal diffusivity was measured with a laser flash analyzer (LFA). The thermal diffusivity (α) was determined by monitoring the temperature change of the upper surface of sample with a pulsed laser applied to the bottom. The thermal diffusivity of GPOSs was calculated based on eq 2:

$$\kappa = \alpha \times \rho \times C_p \tag{2}$$

where ρ is density and C_p is the specific heat capacity. It is widely accepted that the specific heat capacity during phase transition experiences an extra elevation due to the additional energy required for storage rather than transfer.[43] To eliminate the heat storage effect, the nonphase-change heat capacity is determined by the interpolation of the DSC curve.[44]

Contact Thermal Resistance

The contact thermal resistance was measured at 55 °C under pressures of 40−60 psi, according to the ASTM D5470 standard. The GPOS samples with different thicknesses were used to calculate R_{total} and R_c based on eq 3 and eq 4:

$$R_{total} = \frac{T_h - T_c}{Q} \tag{3}$$

$$R_{total} = \frac{BLT}{\kappa_{TIM}} + R_{contact} \tag{4}$$

where T_h is temperature of the heater, T_c is the temperature of the heat sink, Q is the heating power, and BLT is the thickness of samples.

Hot Bridge Experiment

Two ends of GF and GPOS lamellar strips were set between the copper heater and the heat sink, with a suspended distance of about 4 cm. The samples were tightly fixed onto the copper using silver glue to reduce potential thermal resistance. One side of the copper frame (heat sink) was fixed to a lifting platform. By controlling the lifting platform, the other side could instantaneously contact the constant-temperature heater. Thermal grease was applied to the heater to guarantee proper heat contact between the heater and the copper block. An IR camera was placed above the hot bright setup to record the temperature changes, and all samples were coated with a uniform graphite layer (Kontakt, 76009-AC) to ensure similar infrared emissivity.[52,53]

Numerical Simulations

The simulated model was built based on the structure of GPOS2 with a diameter of ∼1 mm and a height of 200 μm. The heat capacities and thermal conductivities of graphene films and POS were acquired from the DSC curves and thermal diffusion testing. The densities of each component were obtained from multiple measurements. The lower boundary temperature was fixed at the room temperature of 293.15 K, while the upper boundary was heated with an input power of 30 W cm^{-2} for a duration of 60 μs. The calculations were based on Fourier's law, and the heat transfer equations of the static solid materials are listed here:

$$\rho C_p \frac{\partial T}{\partial t} + \nabla q = Q_1 \tag{5}$$

$$q = -\kappa \nabla T \tag{6}$$

where ρ is the density, C_p is the heat capacity at constant pressure, T is the temperature, q is the heat transfer flux, κ is the thermal conductivity, and Q_1 is the applied heat power.

Performance of TIMs

A ceramic heater (Φ9 mm) was used to simulate heat generation in devices, a thermocouple was adopted to record T_{heater}, and a heat sink with liquid cooling was utilized to dissipate heat. GPOSs, commercial carbon fiber thermal pads (WaermTimo WT 5935C-250-65) and a graphene thermal pad (Changzhou Fuxi Technology Co., Ltd.) with a thickness of ∼1 mm were employed and placed between the heater and heat sink under a pressure of 10 psi. To evaluate the cooling performance, power densities ranging from 2 to 30 W cm^{-2} were input, and the corresponding surface temperatures of the heater were recorded.

Characterization

The Raman spectra of PW, POS, and GPOS were analyzed by a Raman spectroscope (WITec alpha300 R, Oxford, Germany) equipped with a 532 nm laser. The microstructure of GPOSs was characterized by using a 3D X-ray Tomography Microscope System (Xradia 620 Versa, Zeiss, Germany). Stress−strain curves were obtained with a dynamic mechanical analyzer (Discovery DMA Q850, TA, USA). The heat capacities were measured using a differential scanning calorimetry instrument (DSC 204 F1, Netzsch, Germany) under an N_2 atmosphere with a heating rate of 10 °C min^{-1} in a temperature range of 10−80 °C. Thermal diffusivity was determined by a laser flash thermal testing instrument (LFA 467 LT, Netzsch, Germany). The measurement of thermal resistance was conducted by utilizing TIM thermal conductivity and resistance measurement equipment (LW-9389, Longwin, China). Infrared images were obtained by an infrared thermographer (H13, Hikvision, China).

■ ASSOCIATED CONTENT

Supporting Information

The Supporting Information is available free of charge at https://pubs.acs.org/doi/10.1021/acsnano.5c17391.

Additional details on the characterization of Raman spectra of POS and PW; leaking weight of POS during thermal cycles; leaking weight of GPOSs under pressure; shape stability testing of PW, POS, and GPOSs; compressive strain−stress curves of GPOSs; cyclic compression performance of GPOSs; vertical thermal diffusivity, density, heat capacity, and total thermal resistance of GPOSs; heat capacity of GF, thermal diffusivity, and thermal conductivity of PW and POS; measurement schematic of the thermal resistance; comparison of thermal performance between GPOS2 and reported TIMs; surface temperature of GPOSs and copper versus heating time; IR images recorded for GF, POS, or GF side of GPOSs and bare POS; temperature difference recorded from GPOS-POS-UP/DOWN; temperature distribution of GPOS2 in the simulation; evaluation of the impact of interfacial thermal resistance on heat transfer; comparison of thermal performance between commercial graphene pad and GPOS3; thermal cycling stability of GPOSs; basic properties of graphene film (PDF)

■ AUTHOR INFORMATION

Corresponding Authors

Chuanren Ye − *Department of Materials Science and Engineering, School of Chemistry and Materials Science, University of Science and Technology of China, Hefei*

https://doi.org/10.1021/acsnano.5c17391
ACS Nano 2026, 20, 2239−2247

*230026, China; orcid.org/0000-0003-3346-8948; Email: ycr19@ustc.edu.cn

Yanwu Zhu − *Department of Materials Science and Engineering, School of Chemistry and Materials Science, University of Science and Technology of China, Hefei 230026, China; State Key Laboratory of Precision and Intelligent Chemistry, University of Science and Technology of China, Hefei 230026, China;* orcid.org/0000-0002-7505-1502; Email: zhuyanwu@ustc.edu.cn

Authors

Xiaoqian Teng − *Department of Materials Science and Engineering, School of Chemistry and Materials Science, University of Science and Technology of China, Hefei 230026, China*

Shantao Zhang − *Department of Materials Science and Engineering, School of Chemistry and Materials Science, University of Science and Technology of China, Hefei 230026, China*

Complete contact information is available at: https://pubs.acs.org/10.1021/acsnano.5c17391

Author Contributions

Y.Z., X.T., and C.Y. conceived the experiments. X.T. conducted the preparation experiments, performed data analysis, and drafted the manuscript. C.Y. and S.Z. helped to analyze the experimental data. C.Y. performed the finite element analysis. C.Y. and Y.Z. supervised the study and revised the manuscript. All authors discussed the results and commented on the manuscript.

Notes

The authors declare no competing financial interest.

■ ACKNOWLEDGMENTS

This work was supported by National Key R&D Program of China (Grant No. 2020YFA0711502), Natural Science Foundation of China (Nos: 52273239, 52325202), the open research fund of Key Laboratory of Precision and Intelligent Chemistry, the Fundamental Research Funds for the Central Universities (WK9990000170 and WK2060250106), and USTC Fellowship (Grant No. F19582025). This work was partially carried out at the USTC Center for Micro and Nanoscale Research and Fabrication. The authors thank Dr. Anfeng Shi and Changsheng Hu (LFA test) at Experimental Center of Engineering and Material Sciences, USTC, and Yu-Xia Bai (DMA test) at Instruments Center for Physical Science, USTC.

■ REFERENCES

(1) Ball, P. Computer engineering: Feeling the heat. *Nature* **2012**, *492*, 174.

(2) Salahuddin, S.; Ni, K.; Datta, S. The era of hyper-scaling in electronics. *Nat. Electron.* **2018**, *1*, 442−450.

(3) Dhumal, A. R.; Kulkarni, A. P.; Ambhore, N. H. A comprehensive review on thermal management of electronic devices. *J. Eng. Appl. Sci.* **2023**, *70* (1), 140.

(4) Razeeb, K. M.; Dalton, E.; Cross, G. L. W.; Robinson, A. J. Present and future thermal interface materials for electronic devices. *Int. Mater. Rev.* **2018**, *63*, 1−21.

(5) Wei, B.; Luo, W.; Du, J.; Ding, Y.; Guo, Y.; Zhu, G.; Zhu, Y.; Li, B. Thermal interface materials: From fundamental research to applications. *SusMater* **2024**, *4*, No. e239.

(6) Dai, W.; Wang, Y.; Li, M.; Chen, L.; Yan, Q.; Yu, J.; Jiang, N.; Lin, C.-T. 2D Materials-Based Thermal Interface Materials: Structure, Properties, and Applications. *Adv. Mater.* **2024**, *36* (37), 2311335.

(7) Chen, X.; Cheng, P.; Tang, Z.; Xu, X.; Gao, H.; Wang, G. Carbon-Based Composite Phase Change Materials for Thermal Energy Storage, Transfer, and Conversion. *Adv. Sci.* **2021**, *8*, 2001274.

(8) Ou, K.; Pang, Y. S.; Yang, M.; Wei, Y. M.; Xie, X. C.; Zeng, X. L.; Zhang, L. C.; Zeng, X. L.; Li, C. C.; Sun, R. Phase-change composite elastomers for efficient thermal management at contact interface. *Compos. Commun.* **2024**, *52*, 102149.

(9) He, H.; Peng, W.; Liu, J.; Chan, X.; Liu, S.; Lu, L.; Le Ferrand, H. Microstructured BN Composites with Internally Designed High Thermal Conductivity Paths for 3D Electronic Packaging. *Adv. Mater.* **2022**, *34* (38), 2205120.

(10) Ouyang, Y. G.; Bai, L. Y.; Tian, H. F.; Li, X. F.; Yuan, F. L. Recent progress of thermal conductive ploymer composites: Al2O3 fillers, properties and applications. *Composites, Part A* **2022**, *152*, 106685.

(11) Balandin, A. A.; Ghosh, S.; Bao, W. Z.; Calizo, I.; Teweldebrhan, D.; Miao, F.; Lau, C. N. Superior thermal conductivity of single-layer graphene. *Nano Lett.* **2008**, *8*, 902−907.

(12) Xu, X.; Pereira, L. F.; Wang, Y.; Wu, J.; Zhang, K.; Zhao, X.; Bae, S.; Tinh Bui, C.; Xie, R.; Thong, J. T.; Hong, B. H.; Loh, K. P.; Donadio, D.; Li, B.; Ozyilmaz, B. Length-dependent thermal conductivity in suspended single-layer graphene. *Nat. Commun.* **2014**, *5*, 3689.

(13) Vallabhaneni, A. K.; Singh, D.; Bao, H.; Murthy, J.; Ruan, X. Reliability of Raman measurements of thermal conductivity of single-layer graphene due to selective electron-phonon coupling: A first-principles study. *Phys. Rev. B* **2016**, *93*, 125432.

(14) Pop, E.; Mann, D.; Wang, Q.; Goodson, K. E.; Dai, H. J. Thermal conductance of an individual single-wall carbon nanotube above room temperature. *Nano Lett.* **2006**, *6*, 96−100.

(15) Kim, P.; Shi, L.; Majumdar, A.; McEuen, P. L. Thermal Transport Measurements of Individual Multiwalled Nanotubes. *Phys. Rev. Lett.* **2001**, *87*, 215502.

(16) Newcomb, B. A. Processing, structure, and properties of carbon fibers. *Composites, Part A* **2016**, *91*, 262−282.

(17) Li, P.; Wang, Z.; Qi, Y.; Cai, G.; Zhao, Y.; Ming, X.; Lin, Z.; Ma, W.; Lin, J.; Li, H.; et al. Bidirectionally promoting assembly order for ultrastiff and highly thermally conductive graphene fibres. *Nat. Commun.* **2024**, *15* (1), 409.

(18) Li, P.; Wang, Z.; Cai, G.; Zhao, Y.; Deng, Z.; Wang, B.; Li, Z.; Ming, X.; Gao, W.; Xu, Z.; Xu, Z. et al.High-performance graphene-based carbon fibres prepared at room temperature via domain folding. *Nat. Mater.*, **2025**, .

(19) Li, A.; Zhang, C.; Zhang, Y.-F. Thermal Conductivity of Graphene-Polymer Composites: Mechanisms, Properties, and Applications. *Polymers* **2017**, *9*, 437.

(20) Yan, Z. Y.; Cai, X. M.; Liang, H. M.; Tang, J. W.; Gou, Q.; Wang, W. Y.; Gao, Y.; Qin, M.; Tan, H. L.; Cai, J. M. Thermally Conductive Epoxy Resin Composites Based on 3D Graphene Nanosheet Networks for Electronic Package Heat Dissipation. *ACS Appl. Nano Mater.* **2024**, *7*, 12644−12652.

(21) Guo, H. C.; Zhao, H. Y.; Niu, H. Y.; Ren, Y. J.; Fang, H. M.; Fang, X. X.; Lv, R. C.; Maqbool, M.; Bai, S. L. Highly Thermally Conductive 3D Printed Graphene Filled Polymer Composites for Scalable Thermal Management Applications. *ACS Nano* **2021**, *15*, 6917−6928.

(22) Liu, P.; Li, X.; Min, P.; Chang, X.; Shu, C.; Ding, Y.; Yu, Z.-Z. 3D Lamellar-Structured Graphene Aerogels for Thermal Interface Composites with High Through-Plane Thermal Conductivity and Fracture Toughness. *Nano-Micro Lett.* **2020**, *13* (1), 22.

(23) Renteria, J.; Legedza, S.; Salgado, R.; Balandin, M. P.; Ramirez, S.; Saadah, M.; Kargar, F.; Balandin, A. A. Magnetically-functionalized self-aligning graphene fillers for high-efficiency thermal management applications. *Mater. Des.* **2015**, *88*, 214−221.

(24) Xu, S.; Wang, S.; Chen, Z.; Sun, Y.; Gao, Z.; Zhang, H.; Zhang, J. Electric-Field-Assisted Growth of Vertical Graphene Arrays and the

Application in Thermal Interface Materials. *Adv. Funct Mater.* **2020**, *30* (34), 2003302.
(25) Zhang, Z.; Lee, C.-S.; Zhang, W. Vertically Aligned Graphene Nanosheet Arrays: Synthesis, Properties and Applications in Electrochemical Energy Conversion and Storage. *Adv. Energy Mater.* **2017**, *7*, 1700678.
(26) Zhu, Y. W.; Qu, B.; Andreeva, D. V.; Ye, C. R.; Novoselov, K. S. Graphene standardization: The lesson from the East. *Mater. Today* **2021**, *47*, 9−15.
(27) Zheng, H. L.; He, P.; Yang, S. W.; Ding, G. Q. Thermally conductive graphene-based films for high heat flux dissipation. *Carbon* **2025**, *233*, 119908.
(28) Huang, K.; Pei, S. F.; Wei, Q. W.; Zhang, Q.; Guo, J. Q.; Ma, C. Q.; Cheng, H.-M.; Ren, W. C. Highly Thermally Conductive and Flexible Thermal Interface Materials with Aligned Graphene Lamella Frameworks. *ACS Nano* **2024**, *18*, 23468−23476.
(29) Dai, W.; Ma, T. F.; Yan, Q. W.; Gao, J. Y.; Tan, X.; Lv, L.; Hou, H.; Wei, Q. P.; Yu, J. H.; Wu, J. B.; Yao, Y. G.; Du, S. Y.; Sun, R.; Jiang, N.; Wang, Y.; Kong, J.; Wong, C. P.; Maruyama, S.; Lin, C.-T. Metal-Level Thermally Conductive yet Soft Graphene Thermal Interface Materials. *ACS Nano* **2019**, *13*, 11561−11571.
(30) Zhang, Y.-F.; Han, D.; Zhao, Y.-H.; Bai, S.-L. High-performance thermal interface materials consisting of vertically aligned graphene film and polymer. *Carbon* **2016**, *109*, 552−557.
(31) Luo, W.; Wei, B.; Luo, T.; Li, B.; Zhu, G. 3D Network of Liquid Metal-Embedded Graphene via Surface Coating for Flexible Thermal Management. *Small* **2024**, *20*, 2406574.
(32) Luo, W.; Zhang, X.; Luo, T.; Li, B.; Wei, B.; Zhang, J.; Zhu, G. A Flexible Thermal Interface Material as the Heat Switch for Solid-State Cooling. *Adv. Funct. Mater.* **2025**, No. e12421.
(33) Dai, W.; Ren, X.-J.; Yan, Q.; Wang, S.; Yang, M.; Lv, L.; Ying, J.; Chen, L.; Tao, P.; Sun, L.; et al. Ultralow Interfacial Thermal Resistance of Graphene Thermal Interface Materials with Surface Metal Liquefaction. *Nano-Micro Lett.* **2022**, *15* (1), 9.
(34) Dickey, M. D. Stretchable and Soft Electronics using Liquid Metals. *Adv. Mater.* **2017**, *29* (27), 1606425.
(35) Li, C. S.; Teng, W. Y.; Hung, L. Y.; Wang, Y. P. Liquid Metal Thermal Interface Material for Packaging: Compatibility and Reactivity Analysis. In*2024 25th International Conference on Electronic Packaging Technology (ICEPT)*; IEEE, 2024. .
(36) Tian, C.; Fu, H. Q.; Wang, Z.; Zhang, Z. X.; Qian, W.; Zhang, H. Z.; Xu, S. Q.; Cao, S. Y.; He, D. P. Deformable surface design of vertical graphene thermal interface materials for efficient heat dissipation. *Cell Rep. Phys. Sci.* **2024**, *5*, 101978.
(37) Jing, Y.; Zhao, Z.; Cao, X.; Sun, Q.; Yuan, Y.; Li, T. Ultraflexible, cost-effective and scalable polymer-based phase change composites via chemical cross-linking for wearable thermal management. *Nat. Commun.* **2023**, *14* (1), 8060.
(38) Hu, Z. P.; Wang, X. L.; Wang, W. R.; Zhang, Z. L.; Gao, H. P.; Mao, Y. L. Raman spectroscopy for detecting supported planar lipid bilayers composed of ganglioside-GM1/sphingomyelin/cholesterol in the presence of amyloid-β. *Phys. Chem. Chem. Phys.* **2015**, *17*, 22711−22720.
(39) McCluskey, P.; Mensah, K.; O'Connor, C.; Gallo, A. Reliable use of commercial technology in high temperature environments. *Microelectron. Reliab.* **2000**, *40*, 1671−1678.
(40) Zhou, T.; Zhang, A. M.; Zhao, C. S.; Liang, H. W.; Wu, Z. Y.; Xia, J. K. Molecular Chain Movements and Transitions of SEBS above Room Temperature Studied by Moving-Window Two-Dimensional Correlation Infrared Spectroscopy. *Macromolecules* **2007**, *40*, 9009−9017.
(41) Fenimore, L. M.; Chen, B. R.; Chen, Y. X.; Barbon, S. M.; Brown, H. A.; Auyeung, E.; Shan, C. L. P.; Torkelson, J. M. Covalent adaptable networks and thermosets of multi-block ethylene/1-octene copolymers made by free-radical processing: Effects of melt flow index and crystallinity on thermomechanical properties and reprocessability. *Eur. Polym. J.* **2024**, *202*, 112661.
(42) Zheng, M. J.; Du, W. M. Phase behavior, conformations, thermodynamic properties, and molecular motion of multicomponent paraffin waxes: A Raman spectroscopy study. *Vib. Spectrosc.* **2006**, *40*, 219−224.
(43) Chen, H.; Yue, Z.; Ren, D.; Zeng, H.; Wei, T.; Zhao, K.; Yang, R.; Qiu, P.; Chen, L.; Shi, X. Thermal Conductivity during Phase Transitions. *Adv. Mater.* **2019**, *31* (6), 1806518.
(44) Blumm, J.; Lindemann, A. Characterization of the thermophysical properties of molten plymers and liquids using the flash technique. In*17th European Conference on Thermophysical Properties, High Temperatures*; High Pressures2005. 35, 627..
(45) Dai, W.; Lv, L.; Lu, J.; Hou, H.; Yan, Q.; Alam, F.; Li, Y.; Zeng, X.; Yu, J.; Wei, Q.; et al. A Paper-Like Inorganic Thermal Interface Material Composed of Hierarchically Structured Graphene/Silicon Carbide Nanorods. *ACS Nano* **2019**, *13*, 1547−1554.
(46) Tan, X.; Ying, J. F.; Gao, J. Y.; Yan, Q. W.; Lv, L.; Nishimura, K.; Wei, Q. P.; Li, H.; Du, S. Y.; Wu, B.; Xiang, R.; Yu, J. H.; Jiang, N.; Lin, C.-T.; Dai, W. Rational design of high-performance thermal interface materials based on gold-nanocap-modified vertically aligned graphene architecture. *Compos. Commun.* **2021**, *24*, 100621.
(47) Lu, J. H.; Ming, X.; Cao, M.; Liu, Y. J.; Wang, B.; Shi, H.; Hao, Y. Y.; Zhang, P. J.; Li, K. W.; Wang, L. D.; Li, P.; Gao, W. W.; Cai, S. Y.; Sun, B.; Yu, Z.-Z.; Xu, Z.; Gao, C. Scalable Compliant Graphene Fiber-Based Thermal Interface Material with Metal-Level Thermal Conductivity via Dual-Field Synergistic Alignment Engineering. *ACS Nano* **2024**, *18*, 18560−18571.
(48) Dou, Z. L.; Zhang, B.; Xu, P. F.; Fu, Q.; Wu, K. Dry-Contact Thermal Interface Material with the Desired Bond Line Thickness and Ultralow Applied Thermal Resistance. *Acs Appl. Mater. Inter.* **2023**, *15*, 57602−57612.
(49) Chen, C.; He, Y.; Liu, C. Q.; Xie, H. Q.; Yu, W. Comprehensive excellent performance for silicone-based thermal interface materials through the synergistic effect between graphene and spherical alumina. *J. Mater. Sci.: Mater. Electron.* **2020**, *31*, 4642−4649.
(50) Chen, L.; Liu, T. -H.; Wang, X.; Wang, Y.; Cui, X.; Yan, Q.; Lv, L.; Ying, J.; Gao, J.; Han, M.; et al. Near-Theoretical Thermal Conductivity Silver Nanoflakes as Reinforcements in Gap-Filling Adhesives. *Adv. Mater.* **2023**, *35* (31), 2211100.
(51) Ahammed, A. J. S.; Kim, T.; Baik, S. Covalently Functionalized Leakage-Free Healable Phase-Change Interface Materials with Extraordinary High-Thermal Conductivity and Low-Thermal Resistance. *Adv. Mater.* **2023**, *35* (30), 2300956.
(52) Zhang, X.; Guo, Y.; Liu, Y.; Li, Z.; Fang, W.; Peng, L.; Zhou, J.; Xu, Z.; Gao, C. Ultrathick and highly thermally conductive graphene films by self-fusion. *Carbon* **2020**, *167*, 249−255.
(53) Luo, S.; Peng, L.; Xie, Y.; Cao, X.; Wang, X.; Liu, X.; Chen, T.; Han, Z.; Fan, P.; Sun, H.; et al. Flexible Large-Area Graphene Films of 50−600 nm Thickness with High Carrier Mobility. *Nano-Micro Lett.* **2023**, *15* (1), 61.

https://doi.org/10.1021/acsnano.5c17391
ACS Nano 2026, 20, 2239−2247